International Journal on Magnetic Particle Imaging
Vol 3, No 1, Article ID 1703022, 8 Pages

Infinite Science Publishing

Research Article

Comparison of System-Matrix-Based and Projection-Based Reconstructions for Field Free Line Magnetic Particle Imaging

Serhat Ilbey[a,b,c,*] · Can Barış Top[a] · Alper Güngör[a] · Tolga Çukur[b,c,d] · Emine Ulku Saritas[b,c,d] · Hüseyin Emre Güven[a]

[a] ASELSAN Research Center, Ankara, Turkey
[b] Department of Electrical and Electronics Engineering, Bilkent University, Ankara, Turkey
[c] National Magnetic Resonance Research Center (UMRAM), Bilkent University, Ankara, Turkey
[d] Neuroscience Program, Sabuncu Brain Research Center, Bilkent University, Ankara, Turkey
[*] Corresponding author, email: silbey@aselsan.com.tr

Received 25 November 2016; Accepted 21 March 2017; Published online 29 March 2017

© 2017 Ilbey; licensee Infinite Science Publishing GmbH
This is an Open Access article distributed under the terms of the Creative Commons Attribution License (http://creativecommons.org/licenses/by/4.0), which permits unrestricted use, distribution, and reproduction in any medium, provided the original work is properly cited.

Abstract

In magnetic particle imaging (MPI), system sensitivity can be enhanced by scanning the sample along a field free line (FFL) instead of a field free point (FFP). FFL MPI data can then be processed via system-matrix or projection-based reconstructions. Here, we compare the relative performance of these two approaches. We assume an ideal FFL (straight and homogeneous), which is translated and rotated in a two-dimensional field-of-view. We simulate the acquired data from a numerical vessel phantom for a broad range of noise levels. For the system-matrix reconstruction, we propose Alternating Direction Method of Multipliers (ADMM) to solve a constrained convex optimization problem. We also analyze the results of the nonnegative fused lasso (NFL) model to compare the performance of ADMM with one of the state-of-the-art system-matrix-based methods. For the projection-based reconstruction, we use the inverse Radon transform formulation with x-space reconstruction. System-matrix-based methods resulted in a higher structural similarity index and contrast compared to the x-space reconstruction method at the expense of longer reconstruction time. Artifacts occurred due to gridding errors for the x-space reconstruction. As expected, ADMM and NFL reconstructions yielded similar image quality.

I. Introduction

Magnetic Particle Imaging (MPI) is a novel imaging method that can be useful for various medical applications such as angiography, stem cell tracking, inflammation imaging, temperature mapping, and tumor detection [1–3]. The amplitude of the MPI signal increases with the number of superparamagnetic nanoparticles encapsulated within a field free region (FFR), where the magnetization response of the nanoparticles is linear [1]. This FFR is generated via a magnetic selection field (SF), and its volume is contracted for higher SF gradients. The FFR in MPI systems typically spans a small spatial region of ellipsoidal shape, referred to as the field free point (FFP). This narrow FFP offers relatively increased spatial resolution in MPI images. However, it also decreases the overall system sensitivity, as fewer nanoparticles can respond to the applied drive field (DF).

Creating a field free line (FFL) instead of an FFP significantly increases the sensitivity of the MPI system [4]. To image a three-dimensional (3D) volume with this approach, the FFL needs to be rotated and trans-

 © 2017 Infinite Science Publishing

lated to sample the entire field-of-view (FOV). While this spatial positioning can be implemented mechanically [5, 6], electronic designs can be preferable in preclinical/clinical imaging setups to avoid mechanical positioning of the imaging system relative to the imaged subject. Recently, an electronically rotated FFL scanner was presented [7] based on an efficient coil design that enabled electronic rotation and translation of the FFL [8].

The data acquired along each FFL is essentially a projection of the SPIO density along that line. This acquisition scheme bears close resemblance to that in Computerized Tomography (CT), where the acquired projection data can be written in the form of a Radon transform. Thus, a common reconstruction method for FFL MPI scans - known as x-space reconstruction - is based on the well-known projection reconstruction technique for CT images [7, 9, 10].

During x-space reconstruction, the MPI signal is first compensated for line velocity and particle relaxation, and deconvolved with the system's transfer function. The image can then be reconstructed using an inverse Radon transform [7]. In this x-space-based method [9], the magnetic field gradient is assumed to be independent of scan position and constant along the FFL. In addition, the FFL is assumed to be a straight line, although deviations can occur in practice [5, 11, 12].

An alternative reconstruction to process MPI data is based on the system matrix [1, 13]. In this method, the MPI signal from a small source object located at a single voxel is recorded. Measurements are repeated as the source object is swept across each voxel within the FOV. These calibration measurements are used to construct the system matrix. The main experiment is conducted afterwards, and MPI signals are recorded from the actual object of interest. MPI images are finally reconstructed by solving a linear system of equations comprising the system matrix and the signal measurements. The system-matrix approach inherently accounts for field imperfections, and thus it has the potential to improve reconstruction accuracy. At the same time, it requires the solution of regularized inverse problems either via direct or iterative techniques, which are computationally demanding relative to the projection-based method [14]. Algebraic Reconstruction Technique (ART) is a direct technique of common choice due to its rapid convergence behavior [14, 15]. Recently, nonnegative fused lasso (NFL) has been proposed as an improved method for edge preservation [16].

In this study, we compare the projection-based and system-matrix reconstruction techniques for an FFL-MPI system, in terms of both reconstruction time and quality. For the system-matrix reconstruction, we propose the use of an efficient Alternating Direction Method of Multipliers (ADMM) algorithm, which is based on an Augmented Lagrangian Method (ALM) [17]. ADMM is a recently re-invented technique that solves a given problem by dividing it into smaller sub-problems using a quasi-Newton approach. Moreover, the algorithm includes augmented Lagrangian terms that yield fast convergence speed. We also implement the system-matrix-based NFL algorithm [16], and compare the results with the ADMM approach.

II. Methods

An ideal FFL with an SF of 2 T/m was generated and scanned in a 48 mm × 48 mm FOV with a 25 kHz DF frequency (see Fig. 1). The pixel size used in the simulation was 300 μm × 300 μm. The FFL was rotated in 3-degree angular steps. A particle diameter of 25 nm was assumed. The transmit pulse width was 280 μs. A DF was applied to translate the FFL in the direction orthogonal to it. For simplicity, the DF was chosen as 60 mT, large enough to cover the entire FOV in a single cycle, releasing the need to adjust the amplitude offsets of the partial FOV images [2].

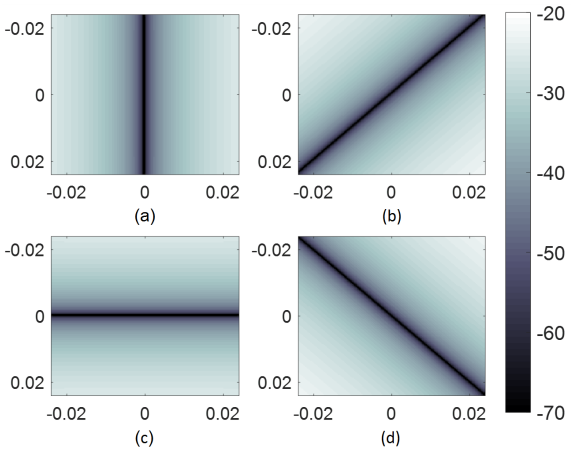

Figure 1: Selection field (dB) used in the simulations shown for (a) 0, (b) 45, (c) 90 and (d) 135 degrees FFL angles. Horizontal axis: x (m), vertical axis: y (m).

The MPI signal at each rotation angle $\theta_k (k: 1,\ldots,K)$ was calculated using the MPI signal equation [10]:

$$s(\theta_k,t) = -\frac{\partial}{\partial t}\int_{-\infty}^{\infty}\int_{-\infty}^{\infty}\mu_0 \boldsymbol{c}(x,y)\ldots \\ \ldots\mathscr{L}\left(\beta\left|\boldsymbol{H}(x,y,t)\right|\right)\frac{\boldsymbol{H}(x,y,t)}{\left|\boldsymbol{H}(x,y,t)\right|}\cdot\boldsymbol{q_r}\,\mathrm{d}x\,\mathrm{d}y\,, \tag{1}$$

where $\boldsymbol{c}(x,y)$ is the magnetic particle distribution inside the FOV. $\mathscr{L}$ is the Langevin function. $\beta = M_{\mathrm{sat}}/k_B T$, with M_{sat}: saturation magnetization $(0.6/\mu_0)$, V: magnetic particle volume, k_B: Boltzmann constant $(1.38\cdot10^{-23})$, T: particle temperature (305 K). $\boldsymbol{q_r}$ denotes the sensitivity of the receiving coils, which are assumed to be homogeneous. $\boldsymbol{H}(x,y,t)$ is the total magnetic field at position

10.18416/ijmpi.2017.1703022
© 2017 Infinite Science Publishing

(x, y) and time t.

To mimic realistic imaging conditions, the signal was convolved with an exponential relaxation kernel $r(t)$ with $\tau = 1\,\mu$s [7, 18], and additive white Gaussian noise, $n(t)$, was added to the time domain signal with *awgn* function of MATLAB (The MathWorks, Inc., MA, USA):

$$S_r(\theta_k, t) = S(\theta_k, t) * r(t) + n(t), \tag{2}$$

where

$$r(t) = \frac{1}{\tau} \exp^{-t/\tau} h(t), \tag{3}$$

with $\tau > 0$ as a relaxation time, $h(t)$ is the unit step function.

The received signal $S_r(\theta_k, t)$ was sampled at 10 MHz rate. A numerical binary vascular tree phantom (160 × 160 pixels) including three stenosis regions (see Fig. 2) was imaged using the presented FFL MPI configuration (see Fig. 1) with three different reconstruction methods.

Figure 2: Numerical vessel phantom used in the simulations. Arrows show the regions with stenosis.

Images of the vessel phantom were reconstructed using frequency components up to 1.25 MHz (i.e., using 50 harmonics). As required in practice, to remove the direct feedthrough signal from the transmit coil, the frequency components up to and including the first harmonic were filtered out prior to reconstruction. All algorithms and the simulator were implemented on MATLAB running on an Intel® Xeon® 2.4 GHz CPU 2620v3 12 cores, workstation (2 processors) with 64 GB RAM. The reconstructed images were compared with the reference image in terms of structural similarity index measure (SSIM), and normalized root-mean-square error (nRMSE) for various SNR values (noise-free, 30 dB, 20 dB, and 10 dB), where noise power was calculated relative to the norm of the raw received time domain signal before filtering.

II.I. Image Reconstruction with the System-Matrix Method

For system calibration, the received signal's Fourier transform data were stored for a known particle concentration at each pixel position for each rotation angle θ_k. These calibration data form the system matrix, $\boldsymbol{A}$. The system matrix was divided to its Frobenius norm to increase the convergence probability for both ADMM and NFL models. The Fourier transform of the received signal in the imaging experiment was stored in vector $\boldsymbol{b}$. Then, the linear system of equations $\boldsymbol{Ac} = \boldsymbol{b}$ was solved to reconstruct the vectorized particle distribution $\boldsymbol{c}$. Instead of using complex values in the equation system, the real and imaginary parts of $\boldsymbol{A}$ and $\boldsymbol{b}$ were separated and row-wise appended. Compared to complex operations that would yield 4-fold increased computational load, this real-valued formulation only poses a 2-fold increase.

For ADMM reconstruction, the problem was formulated as a constrained optimization minimizing the weighted sum of the total variation (TV) and the l_1 norm of the image. Furthermore, a constraint on positivity of all elements of $\boldsymbol{c}$ was added. This constraint was implemented in the ADMM algorithm using an objective function $I_{\text{pos}}(\boldsymbol{c})$, which is the indicator function of all-positive elements such that its value is zero if all elements of $\boldsymbol{c} \geq 0$, and infinite if any element is negative. The problem can therefore be expressed as:

$$\begin{aligned} &\operatorname{argmin}_{\boldsymbol{c}} \alpha_1 \|\boldsymbol{c}\|_1 + \alpha_2 \mathrm{TV}(\boldsymbol{c}) + I_{\text{pos}}(\boldsymbol{c}) \\ &\text{subject to } \|\boldsymbol{Ac} - \boldsymbol{b}\|_2 \leq \epsilon, \end{aligned} \tag{4}$$

where ϵ is the Euclidian norm of the presented noise, $\boldsymbol{b}$ is the received signal and TV is defined as:

$$\mathrm{TV}(\boldsymbol{c}) = \sum_{i,j} \sqrt{\left(\boldsymbol{c}_{i+1,j} - \boldsymbol{c}_{i,j}\right)^2 + \left(\boldsymbol{c}_{i,j+1} - \boldsymbol{c}_{i,j}\right)^2}. \tag{5}$$

Unlike [16], here we used an isotropic TV definition [19]. The data fidelity constraint in (4) was also cast as a cost function such that the value of the indicator function is zero if the constraint is satisfied, and infinity otherwise. The resulting optimization problem was solved with the hybrid cost function presented in (4), using ADMM [17].

ADMM solves a given problem by dividing it into smaller sub-problems. The pseudocode of the algorithm is given below, where $\boldsymbol{A}$ represents the system matrix, μ is the step size, and $\boldsymbol{b}$ is the received signal. Here, $m = 2$ because a weighted sum of 2 cost functions are proposed as TV and l_1 norm.

Moreau proximal mapping functions associated with each linearly separable cost function are required to solve the problem defined in (4). Here we provide proximal operators for each function. Proximal mapping for l_1 norm with weighting is given as:

$$\Psi_{\|\boldsymbol{c}\|_1/\alpha_1}(s) = \mathrm{soft}(\boldsymbol{c}, 1/\alpha_1), \tag{6}$$

where $\mathrm{soft}(y, \tau)$ is the element-wise application of soft-thresholding function:

$$\mathrm{soft}(\boldsymbol{c}, 1/\alpha_1) = \mathrm{sign}(\boldsymbol{c}) \cdot \max(|\boldsymbol{c}| - 1/\alpha_1, 0). \tag{7}$$

© 2017 Infinite Science Publishing

Algorithm 1 ADMM with Hybrid Cost Function [17]

1: Set iteration variable $n=0$, choose step size $\mu>0$
Initialize $\boldsymbol{z}_0^{(i)}$, $\boldsymbol{d}_0^{(i)}$
2: **Repeat**
3: $\hat{\boldsymbol{c}}_{n+1}=\left(m\boldsymbol{I}+\boldsymbol{A}^H\boldsymbol{A}\right)^{-1}\left(\boldsymbol{A}^H\left(\boldsymbol{z}_n^{(0)}+\boldsymbol{d}_n^{(0)}\right)+\ldots \cdots\sum_{i=1}^{m}\left(\boldsymbol{z}_n^{(i)}+\boldsymbol{d}_n^{(i)}\right)\right)$
4: $c_{n+1}=\hat{\boldsymbol{c}}_{n+1}\cdot(\hat{\boldsymbol{c}}_{n+1}>0)$
5: **for** $i=1,\ldots,m$ **do**
6: $\boldsymbol{z}_{n+1}^{(i)}=\Psi_{\alpha_i\phi_i/\mu}\left(\boldsymbol{c}_{n+1}-\boldsymbol{d}_n^{(i)}\right)$
7: $\boldsymbol{d}_{n+1}^{(i)}=\boldsymbol{d}_n^{(i)}+\boldsymbol{z}_{n+1}^{(i)}-\boldsymbol{c}_{n+1}$
8: **end for**
9: $\boldsymbol{z}_{n+1}^{(0)}=\Psi_{\boldsymbol{I}_{E(\epsilon,\boldsymbol{I},\boldsymbol{b})}}\left(\boldsymbol{A}\boldsymbol{c}_{n+1}-\boldsymbol{d}_n^{(0)}\right)$
10: $\boldsymbol{d}_{n+1}^{(0)}=\boldsymbol{d}_n^{(0)}+\boldsymbol{z}_{n+1}^{(0)}-\boldsymbol{A}\boldsymbol{c}_{n+1}$
11: $n\leftarrow n+1$
12: **Until** some stopping criterion is satisfied.

Proximal mapping for TV with weighting α_2 is calculated using Chambolle projections as in [19]. For the constraint function $\|\boldsymbol{A}\boldsymbol{c}-\boldsymbol{b}\|_2\le\epsilon$, proximal mapping is as follows:

$$\Psi_{l_{E(\epsilon,\boldsymbol{I},\boldsymbol{b})}}(\boldsymbol{s})=\begin{cases}\boldsymbol{s}, & \text{if } \|\boldsymbol{s}-\boldsymbol{b}\|_2\le\epsilon\\ \boldsymbol{b}+\epsilon\frac{(\boldsymbol{s}-\boldsymbol{b})}{\|\boldsymbol{s}-\boldsymbol{b}\|_2}, & \text{if } \|\boldsymbol{s}-\boldsymbol{b}\|_2>\epsilon\end{cases} \tag{8}$$

where $l_{E(\epsilon,\boldsymbol{I},\boldsymbol{b})}$ represents the indicator function of the feasible set $E(\epsilon,I,\boldsymbol{b})$. Positivity constraint can be forced at the least squares step of the algorithm (see step 4, Alg. 1).

For comparison purposes, the NFL reconstruction was implemented on MATLAB using the previously presented algorithm in [16]. The problem formulation for the NFL approach is as follows:

$$\text{argmin}_{\boldsymbol{c}}\beta\|\boldsymbol{c}\|_1+\alpha\text{TV}_P(\boldsymbol{c})+\frac{1}{2}\|\boldsymbol{A}\boldsymbol{c}-\boldsymbol{b}\|_2^2+I_{pos}(\boldsymbol{c}), \tag{9}$$

where $\text{TV}_P(\boldsymbol{c})$ is defined as [20]:

$$\text{TV}_P(\boldsymbol{c})=\sum_{p=1}^{P}\sum_{ij}w_p|\boldsymbol{c}_{ij}-\boldsymbol{c}_{(i,j)+\mathcal{N}(p)}|. \tag{10}$$

Here, P is number of directions. The directions and weights (w_p) for each direction is [21]:

$$\begin{aligned}\mathcal{N}=\{&(1,0),(0,1),(1,1),(1,-1),\\ &(2,1),(2,-1),(1,2),(1,-2)\}\end{aligned} \tag{11}$$

$$w_s=\begin{cases}\sqrt{5}-2 & ,s=1,2\\ \sqrt{5}-\frac{3}{2}\sqrt{2} & ,s=3,4\\ \frac{1}{2}(1+\sqrt{2}-\sqrt{5}) & ,s=5,6,7,8\end{cases} \tag{12}$$

The same implementation of the taut string algorithm [22] was used to solve (9) as in the case of [16]. It is worth mentioning that although the problem model stated for ADMM is very similar to the one in NFL, the TV formulations are different.

In ADMM solution, we scaled the ϵ value with the noise level. The ADMM parameters α_1 and α_2, and NFL parameters α and β were separately adjusted to attain the optimal SSIM values. ϵ, α, and β values used for each SNR value are given in Tab. 1.

As a stopping criterion for the above solutions,

$$\|\boldsymbol{c}_{n-1}-\boldsymbol{c}_n\|_2/\left(\|\boldsymbol{c}_n\|_2+10^{-3}\right)<tol \tag{13}$$

was used, where n is the iteration number and tol was set as $1\cdot10^{-5}$. Maximum number of iterations was set to $5\cdot10^3$ for ADMM and $1\cdot10^4$ for NFL solutions. With these parameters, the SSIM values of the reconstructed images converged before reaching the maximum number of iterations or upon satisfying the stopping criterion.

For both ADMM and NFL solutions, least square solution of the problem was given as an initial solution to start the reconstruction algorithms.

Table 1: The parameters for ADMM and NFL that result in the best SSIM performance at each SNR value.

		Noise free	30 dB	20 dB	10 dB
ADMM	ϵ	0.1	0.68	2.14	6.74
	α_1	0.96	0.96	0.96	0.85
	α_2	0.04	0.04	0.04	0.15
	μ	90	80	75	40
NFL	α	$2\cdot10^{-5}$	$2\cdot10^{-5}$	$7\cdot10^{-5}$	$7\cdot10^{-4}$
	β	$9\cdot10^{-4}$	$1\cdot10^{-3}$	$6\cdot10^{-4}$	$1\cdot10^{-3}$
	λ	1	1	1	1
	γ	1.8	1.8	1.8	1.8

II.II. Image Reconstruction with the Projection-Based Method

For the inverse Radon transform (IRadon) reconstruction, the received signal can be re-formulized as follows:

$$S_r(\theta_k,t)=(D\Lambda'(t)(\hat{m}(v)*R(\boldsymbol{c})(\theta_k,v)))*r(t), \tag{14}$$

where $\hat{m}(v)$ is the convolution kernel as

$$\hat{m}(v)=m\frac{\mathrm{d}}{\mathrm{d}v}\mathscr{L}\left(\frac{\mu_0 G v m}{k_B T}\right), \tag{15}$$

$\mathscr{L}$ is the Langevin function, D is the amplitude of DF, $\Lambda(t)=\sin(2\pi f_0 t)$ is the excitation function of the DF, f_0 is the DF frequency, $R(\boldsymbol{c})$ is the Radon transform of the sampled image, and m is the magnetic moment per mass unit of the sample. $r(t)$ is the relaxation kernel [7, 18].

© 2017 Infinite Science Publishing

For the reconstruction process, we first took the average of the DF cycles of the received signal, and passed the average signal through a Wiener filter to remove the effect of relaxation. Then, the time domain signal was divided by the FFL velocity, and transformed to the spatial domain using interpolation. For interpolation, we used the *interp1* function of MATLAB using piece-wise cubic hermit interpolating polynomial (*pchip*). Next, the signal was deconvolved with the convolution kernel using a Wiener filter. This process was repeated for all rotation angles. Finally, the image was reconstructed with inverse Radon transform using the *iradon* function in MATLAB. Details of these reconstruction procedures were previously presented in [7, 10]. IRadon images can contain negative values as a side-effect of various filtering and deconvolution steps. These values were set to zero, and images were then normalized to a maximum of one.

II.III. Image Metrics

SSIM and nRMSE metrics were used to quantitatively compare the reconstructed images. The SSIM metric was calculated using the *ssim* function in MATLAB with default input parameters. The nRMSE was calculated using the standard definition:

$$\mathrm{nRMSE} = \frac{\sum_{i=1}^{W} \sqrt{\frac{1}{W}\left(c_{rec,i} - c_{ref,i}\right)^2}}{\max(\boldsymbol{c}_{rec}) - \min(\boldsymbol{c}_{rec})}, \qquad (16)$$

where $\boldsymbol{c}_{rec}$ is the reconstructed image vector, $\boldsymbol{c}_{ref}$ is the reference image vector, and W is the number of pixels in the image. All reconstructed images were normalized to a maximum of one prior to metric calculations.

III. Results

Figs. 3–6 show the SSIM and nRMSE results for the ADMM and NFL methods as a function of cumulative computation time, which is measured with *cputime* function in MATLAB, for noise-free case, 30 dB SNR, 20 dB SNR and 10 dB SNR values. The corresponding images are given in Fig. 7. The SSIM and nRMSE parameters of the reconstructed images are tabulated for all noise levels in Tab. 2 and Tab. 3, respectively.

For the IRadon solution, reconstruction time was 15.6 ms for all SNR values. Since this is a direct algorithm, its reconstruction time is significantly shorter and depends only on the size of the data.

For all noise levels, the images reconstructed with ADMM and NFL, and the resulting quality metrics (SSIM and nRMSE) are similar. Both system-matrix methods clearly depict vessel edges, yet the IRadon method yields blurry images and lower SSIM values as shown in Fig. 7. Furthermore, gridding artifacts in IRadon reconstructions are visible at all SNR values and residual artifacts

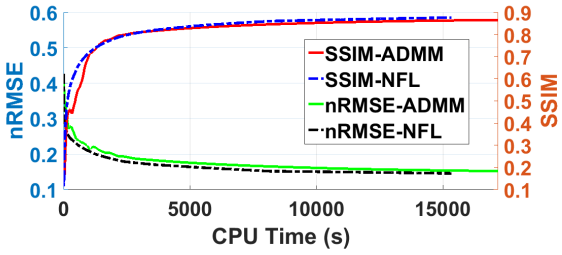

Figure 3: SSIM and nRMSE as a function of cumulative computation time for the noise-free case.

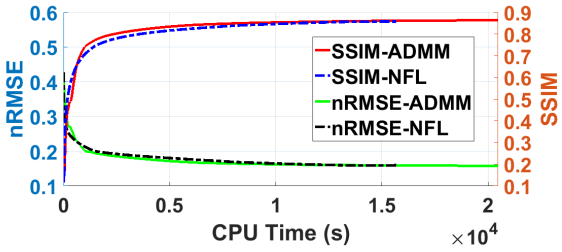

Figure 4: SSIM and nRMSE as a function of cumulative computation time at 30 dB SNR.

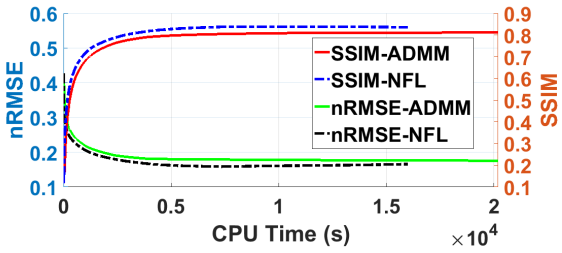

Figure 5: SSIM and nRMSE as a function of cumulative time at 20 dB SNR.

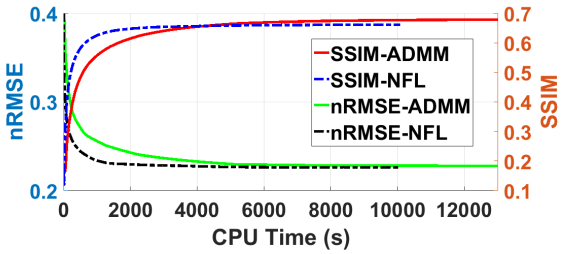

Figure 6: SSIM and nRMSE as a function of cumulative computation time at 10 dB SNR.

reach the intensity level of the vessels themselves at 10 dB. These residual artifacts result in a poor contrast in IRadon images compared to the system-matrix-based images.

In the presence of noise, ADMM and NFL show similar SSIM and nRMSE performance as a function of CPU time. For both methods, convergence is reached within similar total CPU time. These results are expected be-

 © 2017 Infinite Science Publishing

Table 2: SSIM of final images.

	Noise free	30 dB	20 dB	10 dB
ADMM	0.87	0.86	0.81	0.68
NFL	0.88	0.86	0.84	0.66
IRADON	0.55	0.55	0.54	0.42

Table 3: nRMSE of final images.

	Noise free	30 dB	20 dB	10 dB
ADMM	0.15	0.16	0.18	0.23
NFL	0.15	0.16	0.17	0.23
IRADON	0.27	0.27	0.27	0.30

cause ADMM and NFL use nearly identical problem formulations apart from the differences in the definitions of the TV term.

IV. Discussion

The system-matrix-based ADMM and NFL methods outperformed the IRadon method, which yielded blurry images, in terms of both SSIM and nRMSE. On the other hand, the IRadon method was very fast, resulting in reconstructions on the order of 10-20 ms. As the problem complexity of the ADMM and NFL solutions are similar, they showed similar convergence behavior.

While SSIM and nRMSE performance metrics are used commonly for image evaluation, purely quantitative inspections can be misleading without confirmation via visual inspection. In particular, SSIM and nRMSE are global metrics that do not reflect the type of reconstructions errors contained (e.g., blurring, noise, block artifacts). Further studies are needed to identify performance metrics that most highly correlate with the radiological evaluations in a clinical setting.

There were three small regions with stenosis included in the numerical phantom tested here. By means of visual inspection, it was observed that system-matrix-based methods (ADMM and NFL) result in higher contrast near stenotic regions compared to projection-based (IRadon) reconstructions at all SNR values. In this study, we selected the reconstruction parameters (α_1 and α_2 vs. α and β) freely to optimize the SSIM value in each method. Although the formulation of the system-matrix solutions was similar for the ADMM and NFL approaches, the relative weightings assigned to l_1 norm and TV penalties were different. This is primarily due to the differences in the TV definitions. The TV definition in the NFL method was proposed by Chambolle [20], whereas the definition in ADMM was the isotropic TV [19]. Importantly, the isotropic TV term introduces a two-fold scaling in magnitude that in turn roughly halves the relative TV penalty weights in ADMM.

In the simulations, the whole FOV was covered in a single scan, which required a relatively high DF amplitude and the use of large number of signal harmonics for high resolution. By dividing the FOV into smaller sections, the amplitude of the DF can be decreased and a smaller number of signal harmonics may suffice to obtain a similar resolution [23]. Utilizing a lower DF may actually be necessary to abide by the safety limits of the imaging procedure [24].

The simulations in this study were performed assuming ideal magnetic fields with a constant gradient and linear FFL. In non-ideal conditions, the gradient and the linearity of the FFL would deteriorate with increasing distance from the FOV center, depending on the coil system design. This non-ideality of the FFL results in signal fading and resolution losses [9]. If the FOV is defined as the region where the deviation of FFL gradient and linearity is within "acceptable limits", the results would be similar to the ideal-field conditions. The extent of the "acceptable limits" is out of the scope of this work and is a subject of future studies. The non-linearity of the FFL can be mitigated by using the measured fields in the reconstruction phase. This is already taken into account in the system-matrix approach. For the projection-based reconstruction method, the formulation can be adapted for non-linear FFL paths. The decrease in the gradient amplitude may be a bigger concern as it directly affects the image resolution.

Although the reconstruction times compared to IRadon reconstruction are very high for system-matrix-based ADMM and NFL algorithms, these algorithms can be parallelized to significantly improve their convergence time. Graphics processing units (GPU) may also be used for the same purpose, as these algorithms include many vector-based calculations. Furthermore, reducing system matrix size and system calibration procedure by applying compressive sensing techniques can also improve the convergence time of system-matrix-based methods significantly [25, 26].

In the system-matrix-based reconstruction methods, the least square solution of the problem was given as an initial condition. Performance may be further improved by selecting the starting point as the image reconstructed by the fast IRadon method. A synergistic combination of the system-matrix and projection-reconstruction methods that involves gridding steps followed by iterative reconstructions may improve the convergence speed and quality of the resulting images [27].

V. Conclusion

In this paper, we comparatively analyzed system-matrix and x-space-based reconstruction methods for MPI. The x-space method is computationally fast compared to the

 © 2017 Infinite Science Publishing

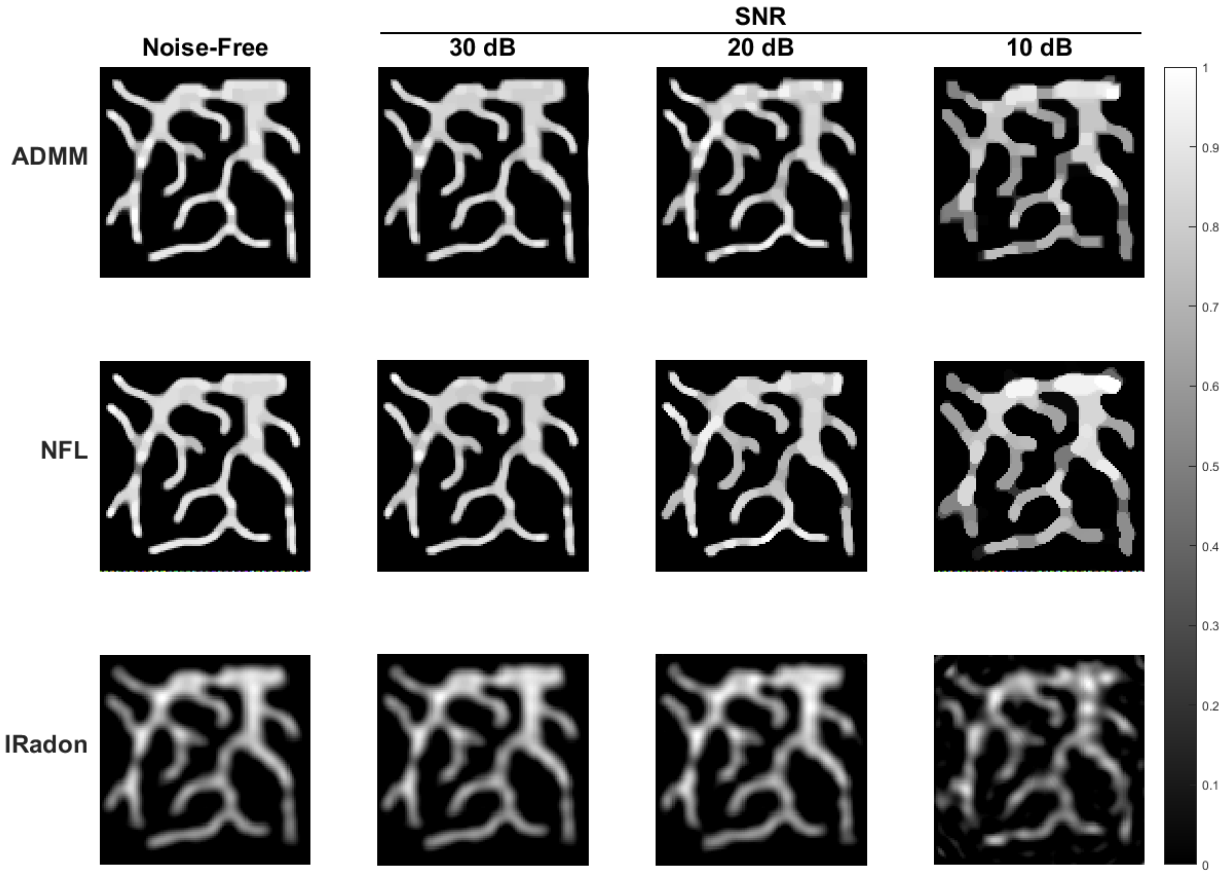

Figure 7: Final images of ADMM, NFL, and IRadon solutions for noise-free, 30 dB SNR, 20 dB SNR, and 10 dB SNR cases.

system-matrix methods and it does not require a time-consuming system calibration scan [25, 26]. However, x-space reconstructions can yield residual artifacts and relatively low contrast. Our results show that system-matrix methods outperform the x-space method in terms of SSIM and nRMSE metrics that reflect enhanced image contrast and artifact suppression.

Acknowledgment

This work was supported by the Scientific and Technological Research Council of Turkey (Project number 9050103). The work of EUS was supported in part by the European Commission through FP7 Marie Curie Career Integration Grant (PCIG13-GA-2013-618834), by the Turkish Academy of Sciences through TUBA-GEBIP 2015 program, and by the BAGEP Award of the Science Academy. The work of TC was supported in part by the European Commission through FP7 Marie Curie Career Integration Grant (PCIG13-GA-2013-618101), by the European Molecular Biology Organization through an Installation Grant (IG 3028), and by the Turkish Academy of Sciences through TUBA-GEBIP 2015 program.

References

[1] B. Gleich and J. Weizenecker. Tomographic imaging using the nonlinear response of magnetic particles. *Nature*, 435(7046):1214–1217, 2005. doi:10.1038/nature03808.

[2] P. W. Goodwill and S. M. Conolly. Multidimensional X-Space Magnetic Particle Imaging. *IEEE Trans. Med. Imag.*, 30(9):1581–1590, 2011. doi:10.1109/TMI.2011.2125982.

[3] C. Stehning, B. Gleich, and J. Rahmer. Simultaneous magnetic particle imaging (MPI) and temperature mapping using multi-color MPI. *Intern. J. Magnetic Particle Imaging*, 2(2):1612001, 2016. doi:10.18416/ijmpi.2016.1612001.

[4] J. Weizenecker, B. Gleich, and J. Borgert. Magnetic particle imaging using a field free line. *J. Phys. D: Appl. Phys.*, 41(10):105009, 2008. doi:10.1088/0022-3727/41/10/105009.

[5] J. J. Konkle, P. W. Goodwill, O. M. Carrasco-Zevallos, and S. M. Conolly. Projection Reconstruction Magnetic Particle Imaging. *IEEE Trans. Med. Imag.*, 32(2):338–347, 2012. doi:10.1109/TMI.2012.2227121.

[6] K. Murase, S. Hiratsuka, R. Song, and Y. Takeuchi. Development of a system for magnetic particle imaging using neodymium magnets and gradiometer. *Jpn. J. Appl. Phys.*, 53(6):067001, 2014. doi:10.7567/JJAP.53.067001.

[7] K. Bente, M. Weber, M. Graeser, T. F. Sattel, M. Erbe, and T. M. Buzug. Electronic field free line rotation and relaxation deconvolution in magnetic particle imaging. *IEEE Trans. Med. Imag.*, 34 (2):644–651, 2015. doi:10.1109/TMI.2014.2364891.

[8] T. Knopp, M. Erbe, S. Biederer, T. F. Sattel, and T. M. Buzug. Efficient generation of a magnetic field-free line. *Med. Phys.*, 37(7): 3538–3540, 2010. doi:10.1118/1.3447726.

 © 2017 Infinite Science Publishing

[9] P. W. Goodwill, J. J. Konkle, B. Zheng, E. U. Saritas, and S. M. Conolly. Projection X-Space Magnetic Particle Imaging. *IEEE Trans. Med. Imag.*, 31(5):1076–1085, 2012. doi:10.1109/TMI.2012.2185247.

[10] T. Knopp, M. Erbe, T. F. Sattel, S. Biederer, and T. M. Buzug. A Fourier slice theorem for magnetic particle imaging using a field-free line. *Inverse Probl.*, 27(9):095004, 2011. doi:10.1088/0266-5611/27/9/095004.

[11] M. Erbe, T. Knopp, T. F. Sattel, and T. M. Buzug. Influence of Magnetic Field Optimization on Image Quality Achieved for Efficient Radon-Based Reconstruction in Field Free Line Imaging in MPI. In *Springer Proceedings in Physics*, volume 140, pages 225–229, 2012. doi:10.1007/978-3-642-24133-8_36.

[12] H. Medimagh, P. Weissert, G. Bringout, K. Bente, M. Weber, K. Gräfe, A. Cordes, and T. M. Buzug. Artifacts in field free line magnetic particle imaging in the presence of inhomogeneous and nonlinear magnetic fields. *Curr. Dir. Biomed. Eng.*, 1(1):245–248, 2015. doi:10.1515/cdbme-2015-0061.

[13] J. Rahmer, J. Weizenecker, B. Gleich, and J. Borgert. Signal encoding in magnetic particle imaging: properties of the system function. *BMC Medical Imaging*, 9(4), 2009. doi:10.1186/1471-2342-9-4.

[14] T. Knopp, J. Rahmer, T. F. Sattel, S. Biederer, J. Weizenecker, B. Gleich, J. Borgert, and T. M. Buzug. Weighted iterative reconstruction for magnetic particle imaging. *Phys. Med. Biol.*, 55(6):1577–1589, 2010. doi:10.1088/0031-9155/55/6/003.

[15] T. Knopp and M. Hofmann. Online reconstruction of 3D magnetic particle imaging data. *Phys. Med. Biol.*, 61(11):N257–N267, 2016. doi:10.1088/0031-9155/61/11/N257.

[16] M. Storath, C. Brandt, M. Hofmann, T. Knopp, J. Salamon, A. Weber, and A. Weinmann. Edge Preserving and Noise Reducing Reconstruction for Magnetic Particle Imaging. *IEEE Trans. Med. Imag.*, 36(1):74–85, 2017. doi:10.1109/TMI.2016.2593954.

[17] H. E. Güven, A. Güngör, and M. Cetin. An Augmented Lagrangian Method for Complex-Valued Compressed SAR Imaging. *IEEE Trans. Comput. Imaging*, 2(3):235–250, 2016. doi:10.1109/TCI.2016.2580498.

[18] L. R. Croft, P. W. Goodwill, and S. M. Conolly. Relaxation in X-Space Magnetic Particle Imaging. *IEEE Trans. Med. Imag.*, 31(12):2335–2342, 2012. doi:10.1109/TMI.2012.2217979.

[19] A. Chambolle. Total Variation Minimization and a Class of Binary MRF Models. In *International Workshop on Energy Minimization Methods in Computer Vision and Pattern Recognition*, pages 136–152, 2005. doi:10.1007/11585978_10.

[20] A. Chambolle. Finite-differences discretizations of the mumford-shah functional. *Esaim Math. Model. Numer. Anal.*, 33(2):261–288, 1999. doi:10.1051/m2an:1999115.

[21] M. Storath, A. Weinmann, J. Frikel, and M. Unser. Joint image reconstruction and segmentation using the Potts model. *Inverse Probl.*, 31(2):025003, 2015. doi:10.1088/0266-5611/31/2/025003.

[22] L. Condat. A Direct Algorithm for 1-D Total Variation Denoising. *IEEE Signal Process. Lett.*, 20(11):1054–1057, 2013. doi:10.1109/LSP.2013.2278339.

[23] L. R. Croft, P. W. Goodwill, J. J. Konkle, H. Arami, D. A. Price, A. X. Li, E. U. Saritas, and S. M. Conolly. Low drive field amplitude for improved image resolution in magnetic particle imaging. *Med. Phys.*, 43(1):424–435, 2016. doi:10.1118/1.4938097.

[24] E. U. Saritas, P. W. Goodwill, G. Z. Zhang, and S. M. Conolly. Magnetostimulation Limits in Magnetic Particle Imaging. *IEEE Trans. Med. Imag.*, 32(9):1600–1610, 2013. doi:10.1109/TMI.2013.2260764.

[25] A. von Gladiss, M. Ahlborg, T. Knopp, and T. M. Buzug. Compressed Sensing of the System Matrix and Sparse Reconstruction of the Particle Concentration in Magnetic Particle Imaging. *IEEE Trans. Magn.*, 51(2):6501304, 2015. doi:10.1109/TMAG.2014.2326432.

[26] A. Weber and T. Knopp. Reconstruction of the Magnetic Particle Imaging System Matrix Using Symmetries and Compressed Sensing. *Adv. Math. Phys.*, 2015:460496, 2015. doi:10.1155/2015/460496.

[27] P. Vogel, T. Kampf, M. A. Rückert, and V. C. Behr. Flexible and Dynamic Patch Reconstruction for Traveling Wave Magnetic Particle Imaging. *Intern. J. Magnetic Particle Imaging*, 2(2):1611001, 2016. doi:10.18416/ijmpi.2016.1611001.

 © 2017 Infinite Science Publishing